MULTILINEAR PETG MATERIAL MODEL IDENTIFIED WITH A NONCONTACT EXTENSOMETER

ONDREJ PIROH[1], JAROSLAV MAJKO[1], JAN MINARIK[1], MILAN VASKO[1], MARIAN HANDRIK[1], MILAN SAGA[1]

[1]Department of Applied Mechanics, Faculty of Mechanical Engineering, University of Zilina, Zilina Slovakia

DOI: 10.17973/MMSJ.2026_11_2026050

ondrej.piroh@fstroj.uniza.sk

This paper presents the identification of a multilinear isotropic hardening material model for PETG produced by fused filament fabrication (FFF) using a noncontact computer vision extensometer. A tensile test was performed on flat specimens with surface line markers, and the marker displacements were measured without contact by tracking them in recorded images. Strain was calculated from these displacements and combined with the measured force to obtain true stress and plastic strain, and ten points of the curve defined the model. The model was implemented in ANSYS Workbench and calibrated against the measured reaction forces of five specimens. The average absolute deviation of the calculated forces was 3.51 %. The results show the procedure provides an effective macroscopic description of the global tensile response of the tested PETG. The model assumes a homogeneous, isotropic material, and its applicability is limited to comparable printing parameters, specimen geometry and loading conditions.

KEYWORDS

multilinear material model, noncontact extensometer, computer vision, Fused Filament Fabrication (FFF), PETG

1 INTRODUCTION

Additive manufacturing technologies have advanced significantly in recent years and are increasingly used across industrial applications, particularly where rapid prototyping or complex geometries are required [Ngo 2018]. Among the most widely used methods is Fused Filament Fabrication (FFF), valued for its low cost and accessible equipment [Turner 2014, Acierno 2023]. However, parts produced by FFF exhibit significant variability in mechanical properties, stemming from filament deposition, anisotropic structure, and sensitivity to printing parameters [Popescu 2018, Hernandez-Alvarez 2026].

PETG (Polyethylene Terephthalate Glycol) is one of the most widely used FFF polymers due to its favorable combination of strength and toughness [Dizon 2018]. Its mechanical behavior, however, is strongly influenced by printing parameters, filament orientation, infill density, and interlayer adhesion quality [Dizon 2018]. Material models should therefore be based on experimental data corresponding to the specific printing configuration used [Wiklo 2025, Paul 2021, Santhosh 2025].

This parameter-dependent variability directly affects the reliability of finite element simulations (FEM), whose accuracy depends on the quality of the input constitutive model [Paul 2021]. Since linear elastic models fail to capture the nonlinear plastic and strain-hardening behavior of thermoplastics [Paul 2021], elastoplastic models derived from experimental data are preferred [Croccolo 2013, Bandinelli 2023]. Such experimentally calibrated models are the foundation of accurate numerical simulation, where experimental data are incorporated directly into FEM constitutive models [Chen 2025]-an approach closely linked to digital twins and model-updating methods, in which numerical models are continuously calibrated against real-world data to improve predictions of service life, failure, and structural behavior [Kessels 2023, Zhang 2020, Ben Amor 2024, Tudorache 2025].

A key requirement for identifying material models is accurate measurement of displacement and strain during mechanical testing. Contact methods such as mechanical extensometers offer high accuracy but are limited in range and can influence measurement conditions through specimen contact [MTS 2022]. Noncontact optical methods avoid this limitation and additionally provide time-resolved data [Meng 2024, Khoo 2016], though typically at the cost of more complex equipment and data processing. Computer vision-based approaches have emerged as a practical balance between accuracy, cost, and ease of implementation [Zhao 2015, Cheng 2024], enabling continuous, sufficiently accurate strain monitoring for constitutive model identification.

The authors previously proposed a low-cost, computer vision-based video extensometer and demonstrated its ability to reliably track displacement and strain in static tests, confirming its suitability for material model identification and simulation verification [Piroh 2025]. While [Piroh 2025] focused on validating the accuracy of the noncontact computer vision extensometer itself, the present work uses this measurement approach to identify a multilinear isotropic hardening material model of FFF-printed PETG and to assess how well a finite element model based on this model reproduces the measured reaction force.

Building on this, the present work identifies and calibrates a multilinear constitutive model for FFF-printed PETG using this noncontact, computer vision-based extensometer. True stress–strain curves obtained from tensile tests and image processing were used to develop a multilinear isotropic hardening model, implemented in ANSYS Workbench [Lee 2020] and calibrated against experimentally measured reaction forces, achieving an average deviation of 3.51 %. The proposed methodology offers a practical route to identifying material parameters for FEM simulations of additively manufactured polymers, supporting more reliable prediction of mechanical behavior, life-cycle analysis, and digital-twin applications where model quality is critical.

2 THEORETICAL BACKGROUND

This chapter outlines the procedure for calculating stress and strain from noncontact extensometer data, followed by a brief characterization of the linear elastic, bilinear isotropic hardening, and multilinear isotropic hardening models used in this work.

2.1 The use of truss elements in the analysis of strain and stress

A noncontact, computer vision-based extensometer yields a set of discrete points tracking surface markers. When arranged along the direction of strain, these points can be treated as nodes of a one-dimensional truss model, allowing strain to be determined for each segment between neighboring reference points.

Let $x_i(t)$, for $i = 1,2,...,n$, denote the reference point coordinates, where n is the total number of nodes. The initial length of the i-th truss element, i.e., the distance between two neighboring points at $t = 0$, is given by equation (1), and its current length at any instant by equation (2).

$$L_{0,i} = x_{i+1}(0) - x_i(0) \quad (1)$$

$$L_i(t) = x_{i+1}(t) - x_i(t) \quad (2)$$

The local engineering strain of the *i*-th element follows from equation (3):

$$\varepsilon_i(t) = \frac{L_i(t) - L_{0,i}}{L_{0,i}} \quad (3)$$

where $\varepsilon_i(t)$ is the engineering strain of that element. A representative strain for the whole analyzed region is obtained as the length-weighted average of the local strains (equation (4)), using the initial element lengths as weights:

$$\varepsilon = \frac{\sum_{i=1}^{n-1} L_{0,i}\varepsilon_i}{\sum_{i=1}^{n-1} L_{0,i}} \quad (4)$$

A schematic of the truss elements defined between the individual lines is shown in **Fig. 1**.

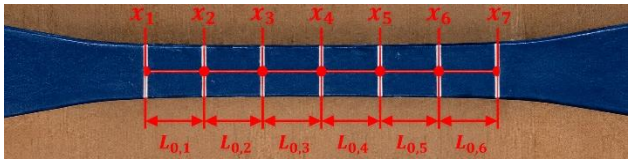


Figure 1. Schematic representation of truss elements on a specimen

With the global strain known, the engineering stress is obtained from the recorded force, equation (5):

$$\sigma_{eng}(t) = \frac{F(t)}{A_0} \quad (5)$$

where $F(t)$ is the instantaneous loading force and A_o the initial cross-sectional area. Since engineering quantities become inaccurate at larger strains, true stress and strain are used for the material model. True strain follows from the global engineering strain ε_{eng} via equation (6), and, assuming constant volume during plastic deformation, true stress from equation (7):

$$\varepsilon_{true} = ln(1 + \varepsilon_{eng}) \quad (6)$$

$$\sigma_{true} = \sigma_{eng}(1 + \varepsilon_{eng}) \quad (7)$$

For elastoplastic behavior, total strain consists of elastic and plastic components (equation (8)), and the plastic component- the key input for elastoplastic material models - is obtained by subtracting the elastic component from the total true strain (equation (9)):

$$\varepsilon_{tot} = \varepsilon_{el} + \varepsilon_{pl} \quad (8)$$

$$\varepsilon_{pl} = \varepsilon_{true} - \frac{\sigma_{true}}{E} \quad (9)$$

where E is the Young's modulus, obtained from the initial slope of the stress-strain curve**.** The plastic strain determined in this way characterizes the permanent strain of the material after the yield point is exceeded. Together with the true stress, this forms the basic input for defining elastoplastic material models used in the finite element method [Chen 2014, Reddy 2013, Lai 1993].

2.2 Material models

Material models define the stress-strain relationship used to predict structural response in FEM simulations [ANSYS 2020]; the choice of model strongly affects the accuracy of the analysis.

This work considers the linear elastic model, bilinear isotropic hardening, and multilinear isotropic hardening.

The linear elastic model (Fig. 2 (a)) assumes a fully reversible, linear stress-strain relationship up to the elastic limit, defined by Young's modulus E and Poisson's ratio μ [ANSYS 2020], and is suitable where no plastic strain occurs.

Bilinear isotropic hardening (Fig. 2 (b)) adds a second, plastic segment beyond the yield strength σ_Y, governed by the tangential modulus E_T. It is simple and computationally efficient, but its single-line plastic segment limits its ability to capture more complex hardening behavior [ANSYS 2020].

Multilinear isotropic hardening (Fig. 2 (c)) extends the bilinear model by representing the post-yield region with multiple linear segments defined by true stress–plastic strain pairs (in ANSYS), typically obtained directly from experimental data. This allows a closer approximation of the actual hardening behavior beyond σ_Y [ANSYS 2020].

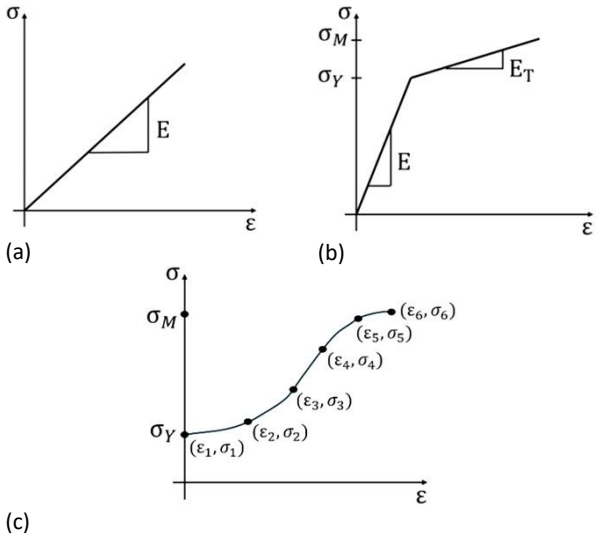


Figure 2. Material models: (a) Linear elastic model, (b) Bilinear isotropic hardening, (c) Multilinear isotropic hardening

3 MEASUREMENT OF DISPLACEMENT ON FLAT SPECIMENS

This chapter describes the experimental methodology used to determine strain during tensile testing using a noncontact, computer vision-based video extensometer, which tracks surface markers to evaluate local strain between reference lines throughout loading [Piroh 2025]. It covers specimen preparation, the tensile test setup, image acquisition, and the workflow used to process the recorded image sequences into input data for the material model.

3.1 Specimen preparation

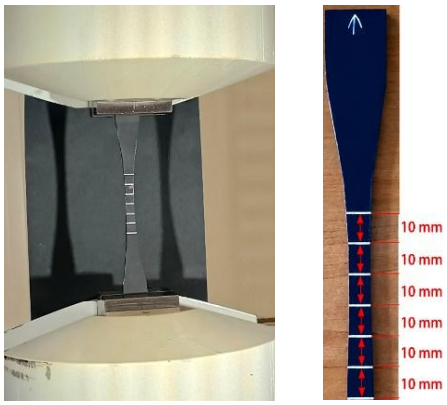
Reliable strain analysis via computer vision requires a specimen surface with clearly distinguishable, trackable regions of interest, particularly in areas prone to damage initiation. Line-shaped markers were therefore applied in the central (narrowed) section of a modified flat specimen geometry, designed — based on the authors' prior experience with FFF thermoplastics — to ensure failure occurred in the gauge section rather than the clamping area, since failure outside the gauge section would not provide relevant data for the material model. The nonstandard geometry and its transition regions may themselves influence the measured response, so the identified model should be understood as representative of this PETG under the tested configuration. This modification was necessary because specimens per ASTM D3039 [ASTM 2017] and ASTM D638-22 [ASTM 2022] did not reliably fail in the central region. The specimen shape is shown in Fig. 3. Only the parameters relevant

for the present analysis are given here: the initial cross-section of the gauge section is 10 × 3.2 mm, giving A_o = 32 mm².



Figure 3. Shape of the used specimens

A total of seven lines (regions of interest) were created on the specimen with a spacing of 10 mm, as shown in **Fig. 4**. The lines were primarily concentrated in the central (narrowed) part of the specimen; however, due to their total number, they also extended into the beginning of the rounded part. This layout made it possible to obtain a comprehensive view of the entire analyzed section and thus provide suitable data for developing the material model. All seven lines shown in Fig. 4 were included in the length-weighted average strain (Eq. 4), including the lines located at the very beginning of the rounded transition region. This placement was intentional: including these lines provided additional insight into the local deformation behavior in this area and allowed the resulting stress–strain curve to more closely reflect the actual response of the specimen, rather than being restricted to an idealized gauge-section-only measurement. Since these lines lie only at the onset of the transition region, where the cross-sectional area is still close to A_o = 32 mm², the resulting difference between including or excluding them from the strain calculation was found to be negligible, and the stress calculation (Eq. 5) based on the constant gauge-section area A_o was therefore retained for the entire analyzed region.



(a) (b)

Figure 4. Lines created on the specimen: (a) specimen clamped in the machine's jaws, (b) close – up of the lines created

Specimens were produced by FFF [Acierno 2023, Popescu 2018] on a Prusa XL printer (0.4 mm nozzle) from PETG [Lakshman 2024, Dolzyk 2019, Sapieta 2023] using a *Concentric* infill pattern, which promotes more uniform stress distribution and load transfer along the loading direction than conventional infill patterns [Agrawal 2023]. Key manufacturing parameters are listed in Tab. 1.

Parameter	Value
Material	PETG
3D printer	Prusa XL
Nozzle diameter	0.4 mm
Layer thickness	0.1 mm
Nozzle temperature	230˚C
Bed temperature	80˚C
Infill structure	Concentric
Infill density	90 %
Build orientation	Flat on the build plate

Table 1. Print parameters

3.2 *Displacement measurements*

Tensile tests were performed on an INOVA-FU-O-160-1260-V1 machine, five specimens under identical conditions (6 mm/min, 20 °C), recorded with a Trust Teza 4K Ultra HD camera [Trust 2026] at 10 fps. The camera was positioned 350 mm from the measured area with its optical axis perpendicular to the specimen surface, following the authors' prior setup [Piroh 2025]; manual focus was used, and pixel displacements were converted to millimeters using the known marker spacing in the pre-deformation reference frame.

Image data were synchronized with the machine's force – displacement data using the maximum pre-failure force as a common time reference, aligning the known sampling rate and frame rate to assign the correct frame to that instant (**Fig. 5**). External LED lighting was used to improve marker contrast without introducing shadows that could cause false detections.



Figure 5. In-situ measurement

The testing machine recorded both jaw displacement and applied force. Jaw displacement was used as the displacement input for the FEM model, since it corresponds directly to the applied boundary condition, allowing consistent comparison of simulated and measured reaction force; the noncontact extensometer was used separately to characterize local strain in the gauge section. Measured data are summarized in Tab. 2.

Specimen:	1	2	3	4	5
Displacement [mm]	3.7	3.43	3.23	3.24	3.35
Force [N]	1306	1274	1300	1289	1312

Table 2. Data measured on the test equipment

Young's modulus was determined from the machine's crosshead-displacement data. The engineering strain was calculated according to equation (3), using the distance between the grips as the reference length (initial length $L_o \approx 179$ mm), and the engineering stress according to equation (5). The compliance of the testing machine and the grips was not considered. For each specimen, the corresponding elastic-range data points — those falling within the 0 – 0.2 % engineering strain interval — were first identified, and a first-order least-squares polynomial (straight-line) fit was then applied to the engineering stress–strain pairs within this range. The slope of the resulting fitted line was taken as the Young's modulus *E* for that specimen. Crosshead displacement was used for consistency with the FEM boundary condition, so that parameter identification and numerical validation relied on the same displacement measure. Results for all five specimens are presented in Table 3.

Specimen:	1	2	3	4	5
Young's modulus [MPa]	3273	3283	3282	3342	3320

Table 3. Calculated values of Young's modulus

The five measured values showed low scatter (standard deviation of 29.6 MPa, i.e., a coefficient of variation of 0.9 %), indicating consistent elastic behavior across the tested specimens; based on this, a mean modulus of 3300 MPa was adopted for the numerical simulations.

Poisson's ratio could not be determined from the available data — the machine provides no transverse measurement, and the line-marker geometry lacks the sensitivity to capture transverse contraction — so a literature value of 0.4 was adopted [Guessasma 2019].

3.3 Evaluation of displacements and the stress-strain curve

Marker positions were extracted from each frame using the detection algorithm described in the authors' previous work [Piroh 2025], which is not repeated here. Relative displacements between neighboring markers were used to form truss elements, from which engineering strains were calculated at each time step and combined into a representative total strain via the length-weighted average of equation (4), then converted to true strain. Engineering stress was calculated by dividing the measured force by the initial cross-sectional area A_o = 32 mm². Engineering stresses were likewise calculated and converted to true stress, yielding the true stress–strain relationship used as the basis for material model selection (Fig. 6). It should be noted that the true stress–strain curve in Fig. 6 does not start from zero stress at zero strain: the force recorded by the testing machine, used to calculate engineering and subsequently true stress (equation 5), was already nonzero at the start of each test, before any prescribed displacement was applied. This initial force offset propagates directly into the stress–strain curve shown in Fig. 6. Its exact cause was not confirmed, though a likely explanation is preload introduced during specimen clamping. The offset was not subtracted from the measured force; it is therefore retained in all stress values and in the averaged curve. Each point on this curve had five available experimental values (one per specimen), combined into a weighted average at each point according to equations (10) and (11), with the weights determined iteratively by manual adjustment to reduce the difference between the simulated and experimentally measured reaction force, considering results from all five tests. Since the aim was to calibrate an effective model rather than to demonstrate its predictive capability on unseen data, no independent validation dataset was used.

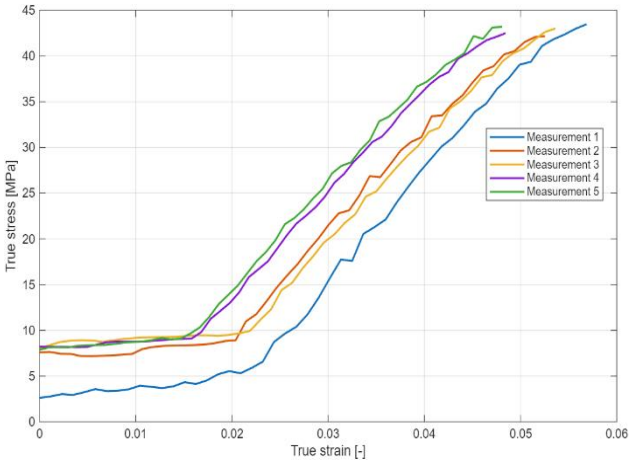


Figure 6. True stress-strain curve

4 SELECTION OF A MATERIAL MODEL

The stress-strain curve clearly shows that the material does not behave as ideally linear elastic: after the initial region, stress increases gradually with plastic strain, and the changing slope indicates hardening — behavior typical of thermoplastics that requires a material model capable of reproducing this nonlinear response.

A bilinear model was considered but would not adequately capture the hardening process across the plastic region. A multilinear isotropic hardening model was therefore chosen, approximating the curve with multiple linear segments for a more accurate representation, while remaining a standard constitutive model directly implementable in ANSYS Workbench. This requires the true stress–plastic strain relationship, calculated from equations (6) – (9) and shown in Fig. 7. The plastic strain was calculated by subtracting the elastic component from the total true strain according to equation (9). Because of the initial stress offset, this gives negative plastic strain at the beginning of each curve; these points were not used, and the curves start at the first point with zero plastic strain. No shift of the strain origin was applied for Fig. 7.

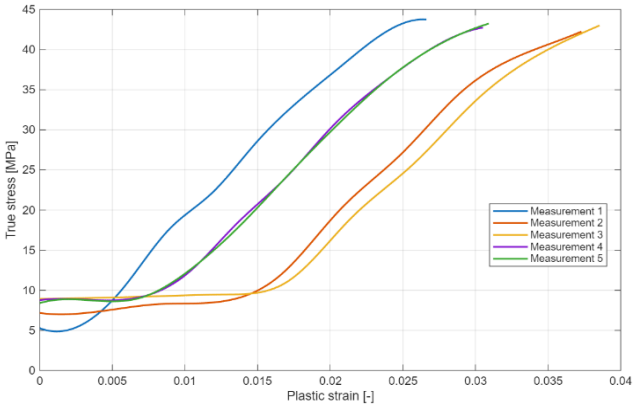


Figure 7. True stress and plastic strain curves

Since five measurements were performed, a single resulting curve was assembled from the weighted average of the individual curves, as described in Section 3.3. The weighted average plastic strain and true stress at each point *k* were calculated using the following equations:

$$\varepsilon_{pl_avg,k} = \frac{\sum_{j=1}^{5} w_j \varepsilon_{j,k}}{\sum_{j=1}^{5} w_j} \tag{10}$$

$$\sigma_{true_avg,k} = \frac{\sum_{j=1}^{5} w_j \sigma_{j,k}}{\sum_{j=1}^{5} w_j} \tag{11}$$

where w_j is the weight of the *j-th* specimen, and $\varepsilon_{j,k}$ and $\sigma_{j,k}$ are the plastic strain and true stress of the *j-th* specimen at tke *k-th* point.

The weights assigned to the five experimental curves were determined through an iterative manual adjustment procedure. For each set of weights, the resulting weighted average curve was used to define the material model in ANSYS Workbench, and the calculated reaction forces were compared with the experimentally measured forces for all five specimens (Tab. 6). The weights were manually adjusted to reduce the deviations between the calculated and measured reaction forces. No explicit mathematical error function or automated optimization algorithm was used. The final weights assigned to the five experimental curves are listed in Tab. 4. The weights therefore act as empirical calibration parameters, and the low weights of specimens 2 and 3 result from this procedure.

Specimen:	1	2	3	4	5
Weight	2	0.1	0.1	1	1

Table 4. The final weight values

As this curve still contains far more points than is practical to use directly, a limited number of representative points was selected as a compromise between approximation accuracy and model simplicity — additional points beyond this offer only marginal accuracy gains while complicating the ANSYS model definition. Ten points were defined at uniform intervals across the plastic strain range, with the corresponding true stress values obtained by linear interpolation of the experimental curve, ensuring a reproducible selection method. The resulting curve is shown in Fig. 8, with the selected points marked by black circles and the resulting curve shown in black. The resulting values are listed in Tab. 5.

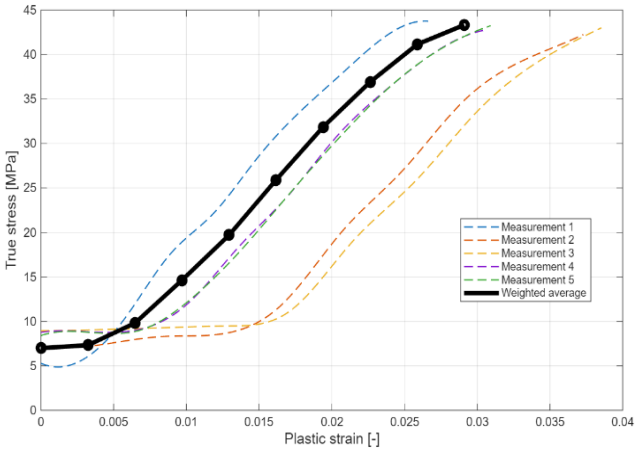


Figure 8. Final true stress and plastic strain curve

Plastic strain [-]	True stress [MPa]
0	7
0.0032	7.32
0.0065	9.81
0.0097	14.63
0.0129	19.70
0.0162	25.91
0.0194	31.86
0.0226	36.92
0.0259	41.15
0.0291	43.33

Table 5. Selected points for the multilinear isotropic hardening model

ANSYS requires the multilinear isotropic hardening table to start at zero plastic strain with the corresponding yield stress. The first point of Tab. 5 (zero plastic strain, 7 MPa) therefore corresponds to the stress of the averaged curve at zero plastic strain and was used as the initial yield stress of the model. Since the initial force offset was not removed from the data, this value includes its influence and should be understood as an effective yield stress of the model.

5 FINITE ELEMENT MODEL DEVELOPMENT

This chapter describes the development of the finite element model in ANSYS Workbench. It covers the mesh, boundary conditions, and load application, as well as the evaluation of the numerical results against the experimental data.

5.1 Finite element mesh and boundary conditions

The finite element model was created as a shell model in ANSYS Workbench. The specimen geometry was reduced to its mid-surface, and a constant thickness of 3.2 mm, equal to the specimen thickness, was assigned as a section property. The shell formulation corresponds to a plane stress state with no variation of stress through the thickness, which is appropriate for thin specimens loaded in uniaxial tension. The model was divided into three parts connected through shared topology to improve both accuracy and correspondence with the experimental configuration. The mesh was generated using a quad-dominant method with linear elements and an element size of 1 mm, consisting predominantly of four-node quadrilateral shell elements with a small proportion of three-node triangular elements (Fig. 9 (a)). Given the magnitude of the calculated deformations, the problem was solved as geometrically nonlinear.

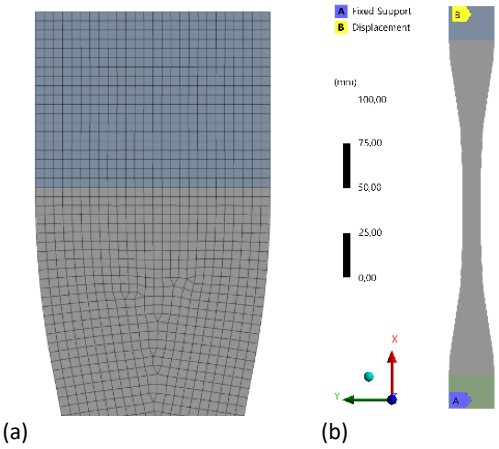


Figure 9. Finite element method setup: (a) detail of finite element mesh, (b) applied boundary conditions

A fixed support was applied at support A, while the prescribed displacement was applied at support B. Given the nonlinear nature of the problem, this displacement was applied gradually in 10 steps, with input values for each simulation taken directly from the final crosshead displacement recorded immediately before specimen failure (mentioned in Tab. 2). The objective was to determine the resulting reaction force at support A.
The material model, defined by the true stress–plastic strain points listed in Tab. 5, was imported into ANSYS Workbench for use in the multilinear isotropic hardening definition.

5.2 Evaluation of measured and calculated values

Five experimental measurements were performed, yielding five simulations with different prescribed displacements. For each, the force measured immediately before specimen failure served as the reference for validating the material model. This point was chosen for the comparison because it reflects the combined effect of prior elastic and plastic deformation and corresponds to the specimen's maximum load-bearing capacity, making it a suitable parameter for assessing the model's ability to reproduce the experimental mechanical response.
Model accuracy was evaluated by directly comparing the ANSYS reaction forces with the measured forces, with the machine-measured force taken as the reference value (Tab. 6). The prescribed displacement is denoted as A, the experimentally measured force as B, the ANSYS reaction force as C, and the deviation as D. The deviation was calculated as the absolute difference between the calculated and the measured force related to the measured force, and its average over the five specimens (3.51 %) is the value reported throughout this article.

Experiment		Simulation	
A [mm]	B [N]	C [N]	D [%]
3.7	1306	1426	9.19
3.43	1274	1336	4.87
3.23	1300	1271	2.23
3.24	1289	1275	1.09
3.35	1312	1310	0.15

Table 6. Comparison of measured and calculated values

As shown in Tab. 6, the deviation exceeded 5 % in one case. This may be partly attributed to the FFF process itself, since the model assumes a homogeneous, isotropic material whereas printed specimens exhibit heterogeneity from layer-by-layer deposition; this was not verified experimentally. The identified model should therefore be understood as an effective macroscopic description of material behavior rather than a microstructure-resolving one. This isotropic approximation was nonetheless considered adequate for the PETG material and printing parameters examined, as it captures the macroscopic mechanical response at a reasonable level of simplification. The resulting model describes PETG behavior within the range of conditions considered here, with parameters reflecting the specific manufacturing and loading conditions used; since the internal structure produced by FFF can significantly affect mechanical properties, the model is applicable to tensile-loaded components with comparable internal structure and manufacturing conditions, and should be re-verified — with parameters re-identified if necessary — for significantly different material arrangements or loading conditions.

As strain increases, so does the force required for further extension — typical of homogeneous materials with approximately uniform properties throughout their volume. In FFF-printed specimens, however, local variations from print orientation, infill geometry, interlayer bond quality, and small voids can cause local damage before the strain level expected in a homogeneous material is reached, contributing to the differences between measured and calculated forces. Despite this, the average deviation of 3.51 % represents very good agreement, indicating that the selected multilinear model reproduces the mechanical behavior of PETG with sufficient accuracy and is suitable as input for FEM simulations of FFF-manufactured PETG components.

The following limitations should be noted. The measured reaction forces show only a limited dependence on the prescribed displacement, while the calculated forces increase more noticeably with it (Tab. 6); part of the reported deviation can therefore be attributed to the scatter of the displacement recorded at specimen failure, rather than solely to the accuracy of the material model. Since the model parameters were calibrated using the same five specimens on which the deviation was subsequently evaluated, the reported values should be interpreted as a measure of calibration quality rather than as an assessment of predictive capability on independent data. The weights of the individual curves were selected manually, without a formal optimization procedure; owing to the low weights of specimens 2 and 3, the identified curve is determined mainly by specimens 1, 4 and 5. Young's modulus was determined from crosshead displacement without correction for machine and grip compliance (Section 3.2), so it is an effective value that may differ from the true material modulus.

The comparison was carried out at a single point of the force response rather than over the full force–displacement curves; this was not the objective of the present study, which was conceived as a methodological foundation for subsequent research and as an initial proof-of-concept assessment of the feasibility of the proposed approach, rather than as a comprehensive predictive validation. As formulated, the model is rate-independent and does not include a failure criterion, which is consistent with its intended use for describing the macroscopic elastoplastic response up to the onset of failure.

6 CONCLUSIONS

This article aimed to identify an effective macroscopic multilinear material model describing the tensile behavior of PETG specimens produced by FFF technology, using a noncontact extensometer based on computer vision. The proposed approach made it possible to determine the displacements of the test specimens without direct contact and, from these, to calculate the strains and stresses used to develop a material model suitable for finite element simulations. Analysis of the obtained stress–strain curves indicated that the behavior of PETG would not be described with sufficient accuracy by either a linear elastic or a bilinear model; a multilinear isotropic hardening model was therefore chosen, approximated using ten representative points.

The identified material model was calibrated by comparing the experimentally measured reaction forces with the FEM simulation results, achieving an average deviation of 3.51 %. As the model parameters were calibrated using the same five specimens on which this deviation was evaluated, this value should be interpreted as a measure of calibration quality rather than as an independent assessment of predictive accuracy; it nonetheless indicates that the proposed methodology can provide an effective macroscopic material model for additively manufactured thermoplastics under comparable printing parameters, specimen geometry and loading conditions. The observed differences between the experimental and numerical results may be partly related to the simplifying assumption of a homogeneous, isotropic material, which does not account for the local inhomogeneities of printed specimens (not verified experimentally), and partly to the scatter of the displacement recorded at specimen failure.

The proposed methodology presents a procedure for developing experimentally calibrated constitutive models applicable to numerical analyses of additively manufactured components with comparable material, manufacturing, and loading conditions. The obtained results should not be generalized to all PETG components manufactured by FFF, as the mechanical response may vary depending on the material, printing parameters, infill strategy, printing orientation, specimen geometry, and loading conditions. Future research will focus on extending the proposed methodology toward the prediction of more complex structural responses, including buckling behavior, as well as on the identification of material models for different infill configurations and other materials produced by additive manufacturing technologies.

ACKNOWLEDGMENTS

This work has been supported by the grant project VEGA 1/0423/23.

REFERENCES

[Acierno 2023] Acierno, D. and Patti, A. Fused Deposition Modelling (FDM) of Thermoplastic-Based Filaments: Process and Rheological Properties—An Overview. Materials, 2023, Vol. 16, No. 24, 7664.

[Agrawal 2023] Agrawal, A.P., et al. An investigation of combined effect of infill pattern, density, and layer thickness on mechanical properties of 3D printed ABS by fused filament fabrication. Heliyon, 2023, Vol. 9, No. 6, e16531.
[ANSYS 2020] ANSYS, Inc. Material Reference. Release 2020 R2. Canonsburg, PA: ANSYS, Inc., 2020.
[ASTM 2017] ASTM International. Standard Test Method for Tensile Properties of Polymer Matrix Composite Materials. ASTM D3039/D3039M-17. West Conshohocken, PA: ASTM International, 2017.
[ASTM 2022] ASTM International. Standard Test Method for Tensile Properties of Plastics. ASTM D638-22. West Conshohocken, PA: ASTM International, 2022.
[Bandinelli 2023] Bandinelli, F., et al. Elasto-plastic mechanical modeling of fused deposition 3D printing materials. Polymers, 2023, Vol. 15, No. 1, 234.
[Ben Amor 2024] Ben Amor, S., et al. Digital twin implementation in additive manufacturing: A comprehensive review. Processes, 2024, Vol. 12, No. 6, 1062.
[Chen 2014] Chen, X. and Liu, Y. Finite Element Modeling and Simulation with ANSYS Workbench. Boca Raton, FL: CRC Press, 2014. ISBN 978-1-4398-7384-7.
[Chen 2025] Chen, B., et al. Finite element model updating for material model calibration: A review and guide to practice. Archives of Computational Methods in Engineering, 2025, Vol. 32, No. 4, pp 2035–2112.
[Cheng 2024] Cheng, W.H., et al. Vision-based algorithm for structural response measurement using movable camera and damage localization. Measurement, 2024, Vol. 232, 114678.
[Croccolo 2013] Croccolo, D., et al. Experimental characterization and analytical modelling of the mechanical behaviour of fused deposition processed parts made of ABS-M30. Computational Materials Science, 2013, Vol. 79, pp. 506–518.
[Dizon 2018] Dizon, J.R.C., et al. Mechanical characterization of 3D-printed polymers. Additive Manufacturing, 2018, Vol. 20, pp 44–67.
[Dolzyk 2019] Dolzyk, G. and Jung, S. Tensile and fatigue analysis of 3D-printed polyethylene terephthalate glycol. Journal of Failure Analysis and Prevention, 2019, Vol. 19, No. 2, pp 511–518.
[Guessasma 2019] Guessasma, S., et al. Printability and tensile performance of 3D printed polyethylene terephthalate glycol using fused deposition modelling. Polymers, 2019, Vol. 11, No. 7, 1220.
[Hernandez-Alvarez 2026] Hernandez-Alvarez, L., et al. Experimental analysis of layer orientation effects in fused filament fabrication (FFF) with PETG: Comparative evaluation of two 3D printers. Journal of Manufacturing and Materials Processing, 2026, Vol. 10, No. 2, 64.
[Kessels 2023] Kessels, B.M., et al. Real-time parameter updating for nonlinear digital twins using inverse mapping models and transient-based features. Nonlinear Dynamics, 2023, Vol. 111, No. 11, pp. 10255–10285.
[Khoo 2016] Khoo, S.W., et al. A review of surface strain and strain measurement using two-dimensional digital image correlation. Metrology and Measurement Systems, 2016, Vol. 23, No. 3, pp. 461–480.
[Lai 1993] Lai, W.M., et al. Introduction to Continuum Mechanics. 3rd ed. Oxford: Butterworth-Heinemann, 1993. ISBN 0-7506-2894-4.
[Lakshman 2024] Lakshman, S.S.V., et al. Evaluation of mechanical properties of 3D printed PETG and Polyamide (6) polymers. Chemical Physics Impact, 2024, Vol. 8, 100491.
[Lee 2020] Lee, H.H. Finite Element Simulations with ANSYS Workbench 2020. Mission, KS: SDC Publications, 2020. ISBN 978-1-63057-401-7.
[Meng 2024] Meng, W., et al. A review: Non-contact and full-field strain mapping methods for experimental mechanics and structural health monitoring. Sensors, 2024, Vol. 24, No. 20, 6573.
[MTS 2022] MTS Systems Corporation. How to Choose an Axial Extensometer. MTS Systems Corporation, 2022, Eden Prairie, MN [online]. 2022-11-07 [cited 2026-06-12]. Available from: www.mts.com/en/articles/materials/choose-extensometer
[Ngo 2018] Ngo, T.D., et al. Additive manufacturing (3D printing): A review of materials, methods, applications and challenges. Composites Part B: Engineering, 2018, Vol. 143, pp. 172–196.
[Paul 2021] Paul, S. Finite element analysis in fused deposition modeling research: A literature review. Measurement, 2021, Vol. 178, 109320.
[Piroh 2025] Piroh, O., et al. Rapid and cost-efficient approach for non-contact measurement in experimental mechanics. Results in Engineering, 2025, Vol. 26, 105408.
[Popescu 2018] Popescu, D., et al. FDM process parameters influence over the mechanical properties of polymer specimens: A review. Polymer Testing, 2018, Vol. 69, pp. 157–166.
[Reddy 2013] Reddy, J.N. An Introduction to Continuum Mechanics. 2nd ed. Cambridge: Cambridge University Press, 2013. ISBN 978-1-107-02543-1.
[Santhosh 2025] Santhosh, S.N.S., et al. Validation of 3-point bending strength of PETG material printed via FDM using FEA. E3S Web of Conferences, 2025, Vol. 648, 01005.
[Sapieta 2023] Sapieta, M., et al. Investigation of the mechanical properties of spur involute gearing by infrared thermography. Applied Sciences, 2023, Vol. 13, No. 10, 5988.
[Trust 2026] Trust. Trust Teza 4K Ultra HD Webcam. Trust International, 2026, Dordrecht, Netherlands [online]. [cited 2026-01-13]. Available from: www.trust.com/en/product/24280-teza-4k-ultra-hd-webcam. Item number 24280.
[Tudorache 2025] Tudorache, L., et al. Current approaches to digital twins in additive manufacturing: A systematic literature review. Progress in Additive Manufacturing, 2025, Vol. 10, No. 12, pp. 10819–10853.
[Turner 2014] Turner, B.N., et al. A review of melt extrusion additive manufacturing processes: I. Process design and modeling. Rapid Prototyping Journal, 2014, Vol. 20, No. 3, pp. 192–204.
[Wiklo 2025] Wiklo, M., et al. Mechanical characterization of FDM 3D-printed components using advanced measurement and modeling techniques. Materials, 2025, Vol. 18, No. 5, 1086.
[Zhang 2020] Zhang, L., et al. Digital twins for additive manufacturing: A state-of-the-art review. Applied Sciences, 2020, Vol. 10, No. 23, 8350.
[Zhao 2015] Zhao, J., et al. Strain measuring technology based on machine vision. In: Proceedings of the 27th

Chinese Control and Decision Conference (CCDC), Qingdao, China, 23–25 May 2015. Piscataway, NJ: IEEE, pp. 5128–5133.

CONTACTS:

Ing. Ondrej Piroh, PhD.
University of Zilina, Faculty of Mechanical Engineering, Department of Applied Mechanics
Univerzitna 8215/1, Zilina 010 26, Slovakia
ondrej.piroh@fstroj.uniza.sk

LICENSE CREATIVE COMMONS:

The article is published under the terms and conditions of the Creative Commons Attribution 4.0 International License (CC BY 4.0).